The Proton-Alpha Instability as a Source of Ion Heating at Earth's Bow Shock

Citation for the original published paper (version of record):
Müller, N., Steinvall, K., Graham, D. et al (2026). The Proton-Alpha Instability as a Source of Ion Heating at Earth's Bow Shock. Journal of Geophysical Research: Space Physics, 131(6).
http://dx.doi.org/10.1029/2026JA035267

AGU ADVANCING EARTH AND SPACE SCIENCES

JGR Space Physics

RESEARCH ARTICLE
10.1029/2026JA035267

Key Points:

- The proton-alpha streaming instability can drive strong waves and significant ion heating at shocks similar to the Earth's bow shock
- The most efficient conversion from bulk kinetic energy to thermal energy occurs when the wavevector is at a 45° angle from the flow
- The impact of the alpha flow speed on the instability and its highly anisotropic plasma heating is visualized through phase-space diagrams

Supporting Information:

Supporting Information may be found in the online version of this article.

Correspondence to:

N. Müller and K. Steinvall,
nils.mueller@awi.de;
konrad.steinvall@chalmers.se

Citation:

Müller, N., Steinvall, K., Graham, D. B., & Pusztai, I. (2026). The proton-alpha instability as a source of ion heating at Earth's bow shock. *Journal of Geophysical Research: Space Physics*, *131*, e2026JA035267. https://doi.org/10.1029/2026JA035267

Received 23 FEB 2026
Accepted 8 JUN 2026

The Proton-Alpha Instability as a Source of Ion Heating at Earth's Bow Shock

N. Müller[1,2], K. Steinvall[1], D. B. Graham[3], and I. Pusztai[1]

[1]Department of Physics and Astronomy, Chalmers University of Technology, Gothenburg, Sweden, [2]Now at Physical Oceanography, Alfred-Wegner-Institute, Bremerhaven, Germany, [3]Swedish Institute of Space Physics, Uppsala, Sweden

Abstract Electrostatic waves are frequently observed at collisionless shocks and are believed to play a key role in energy dissipation. Recent spacecraft observations have identified a proton-alpha instability in the Earth's bow shock as a potential mechanism to dissipate the energy associated with a relative drift between protons and alpha particles, u_α. At plasma parameters relevant to this setting, we investigate the dependence of the evolution of this instability on u_α through particle-in-cell simulations. We find that the instability produces strong ion heating, increasing ion temperatures by factors of two to five. The electrons, in contrast, experience only minimal heating ($\sim 1\%$). The heating is highly anisotropic and is most efficient when the wave vector is at a 45° angle to the alpha flow velocity. To interpret these results, we introduce a geometric model based on Landau resonance interaction bands in velocity space. It explains both the angular dependence and the magnitude of heating through the change in velocity distribution functions. At the same time, the wave properties are consistent with linear theory. Our results demonstrate that the proton-alpha streaming instability can be an important mechanism to convert the bulk kinetic energy of the alphas into ion heating at collisionless shocks.

Plain Language Summary When fast streams of charged particles interact in space, such as near Earth's bow shock, they slow down and heat up. Usually, this happens through plasma instabilities, whereby plasma waves grow and transfer energy between particles. In this study, we focus on a recently observed instability that occurs when alpha particles move faster than protons in a plasma. Through our computer simulations, we study how this instability evolves. In particular, we find that the instability strongly heats the alphas and protons, increasing their temperatures by two to five times, while electrons are barely heated. The heating is the strongest when the plasma waves travel at a 45° angle to the motion of the alpha particles. To understand why, we develop a geometric picture that shows how the particle velocities change due to the wave. We also compare the waves in our simulations with the theoretical predictions and find that they have very similar properties. To summarize, we show that this growing wave heats alpha particles and protons by taking a large portion of the energy of flowing alpha particles. This means that this instability could be important for the Earth's bow shock.

1. Introduction

Collisionless shocks are ubiquitous in plasmas throughout the universe. In the absence of collisions, such shocks rely on other mechanisms related to field-particle interactions to dissipate the energy of the upstream plasma (e.g., Burgess & Scholer, 2015; Kennel et al., 1985). How this dissipation occurs is a central question in the study of collisionless shocks. Two important parameters that play key roles in determining the structure and dissipation mechanisms of collisionless shocks are the ion-to-electrons mass ratio and the charge-to-mass q/m ratio of the different particle species. For example, the large scale separation between the kinetic dynamics of ions and electrons plays an important role in the formation of the cross-shock potential (e.g., Baumjohann & Treumann, 2012; Zank et al., 1996). The decrease in velocity of inflowing ions due to the cross-shock potential is proportional to their q/m as described by the Coulomb force (Graham et al., 2024; Madanian et al., 2024; Pusztai et al., 2018; Yang et al., 2011).

Thermalization through electrostatic instabilities is one potential avenue of energy dissipation at collisionless shocks (e.g., Wilson et al., 2021, and references therein). Large amplitude electrostatic waves have been known to be present at collisionless shocks for a long time (e.g., Fredricks et al., 1970; Rodriguez & Gurnett, 1976). Examples of electrostatic waves observed in the shock context include electron Bernstein waves (Muschietti & Lembège, 2013; Wilson et al., 2010), beam mode waves (Lalti et al., 2025; Onsager & Holzworth, 1990), Langmuir waves at the electron plasma frequency (Cairns et al., 1997; Kellogg, 2003) and its harmonics (Kasaba et al., 2001; Kellogg et al., 2010), and ion acoustic waves (Formisano & Torbert, 1982; Hull et al., 2006). In addition to heating and dissipation, the high-frequency Langmuir waves have been thoroughly studied due to their ability to cause radio emissions (e.g., Cairns et al., 2003; Pulupa & Bale, 2008). The focus of the present paper is a type of ion-acoustic instability.

In-situ observations have shown that ion-acoustic waves are present at shocks for a large range of shock-parameters. For example, ion-acoustic waves have been reported for a range of shock-normal angles (Boldú et al., 2024), from quasi-parallel (Lu et al., 2025), to oblique (Goodrich et al., 2018) and quasi-perpendicular (Formisano & Torbert, 1982; Hull et al., 2006; Vasko et al., 2022). They have also been reported over a wide range of Mach numbers (Goodrich et al., 2018; Graham et al., 2025; Vasko et al., 2022; Wilson et al., 2007). The waves have been found to propagate in a range of directions with respect to the magnetic field, from parallel to perpendicular (Vasko et al., 2022). In the nonlinear stage, they are frequently observed as solitary waves (e.g., Vasko et al., 2018; Wang et al., 2020, 2021). In most of these cases, the waves have been argued to be generated by proton-proton instabilities (e.g., Fuselier et al., 1987; Goodrich et al., 2019; Vasko et al., 2022) or proton-electron instabilities (e.g., Balikhin et al., 2005; Hull et al., 2006). Understanding the instabilities underlying the formation of these waves is crucial, since they play an important role in the energy dissipation (Wilson et al., 2014) and particle heating (Kamaletdinov et al., 2024; Walker et al., 2026) at collisionless shocks.

In recent work, Graham et al. (2025) studied large amplitude ion-acoustic waves found at the ramps and downstream of low-Mach number, quasi-perpendicular shocks observed by the Magnetospheric Multiscale (MMS) spacecraft (Burch et al., 2016). The authors argued that the waves were due to a streaming instability between the protons and alpha particles. In brief, they found that the different q/m of the two ion species causes them to be accelerated differentially by the cross-shock potential, resulting in a relative drift that persists several proton inertial lengths downstream of the shock. This relative motion triggers an ion-acoustic instability, ultimately thermalizing the alpha population at the expense of its relative drift, while simultaneously heating the protons. Graham et al. (2025) used in-situ data, linear theory, as well as one-dimensional, electrostatic particle-in-cell (PIC) simulations to support their conclusions. While the results from the different methods were in good agreement, the 1D nature of their PIC simulation forces the wavevector $\mathbf{k}$ to be parallel to the relative alpha flow $\mathbf{u}_\alpha$. This poses a fundamental limitation when u_α is higher than the phase speed $v_{\mathrm{ph}} = \omega/k$ of the wave, as the most unstable mode then propagates at an increasing angle θ with respect to $\mathbf{u}_\alpha$ according to linear theory (Gary & Omidi, 1987; Graham et al., 2025). Since the interaction between the wave and the particles, and consequently the particle heating, is affected by this angle, the 1D model produces inaccurate results when θ should be > 0. In order to more accurately model the instability and understand its effect on the particle distribution functions, and subsequently on the dissipation of energy, it is essential to study the instability in higher dimensions. Specifically, in the absence of magnetic fields, two spatial dimensions are sufficient to capture the full dynamics of the instability due to the rotational symmetry of the system around the streaming component.

In the present paper, we use PIC simulations to investigate the proton-alpha streaming instability in two spatial and three velocity dimensions. In particular, we are interested in understanding how the instability dissipates energy on a fluid and kinetic level for different values of u_α. To this end, we perform a series of PIC simulations over a range of u_α values, yielding a wide range of θ, and study the resulting plasma heating. In addition, we present a geometrical interpretation of the instability that illustrates clearly how the instability and the resulting waves act to restructure the velocity distribution functions on a kinetic level, thereby heating the plasma.

2. Models and Methods

2.1. Numerical Model

In this study, we use the relativistic and electromagnetic EPOCH PIC code (Arber et al., 2015, 2024) to study the proton-alpha instability in the absence of background magnetic fields. We simulate two spatial and three velocity dimensions. The setup consists of three plasma components: One electron population (subscript e), one proton population (p) and one alpha population (α) with physical mass ratios ($m_{\mathrm{p}}/m_{\mathrm{e}} = 1836$, $m_\alpha/m_{\mathrm{p}} = 4$). We initialize a spatially homogeneous, Maxwellian plasma in the proton-electron rest frame. In this frame, we give the alpha population an initial drift velocity $\mathbf{u}_\alpha = u_\alpha \hat{x}$, to simulate the differential flow generated by the shock-crossing (Graham et al., 2024, 2025).

We simulate in a rectangular domain with periodic boundary conditions. The two-dimensional grid consists of square grid cells with $\Delta x = \Delta y \approx \lambda_D/3$, where $\lambda_D = \sqrt{\epsilon_0 T_e / q_e^2 n_e}$ is the electron Debye length, where q_e, n_e, and T_e are respectively the electron charge, density, and temperature, and ϵ_0 is the vacuum permittivity. The extent of the domain determines the allowed linear wave modes ($\lambda_j = L/j$ with $j \in \mathbb{N}$ at side length L). Thus, the domain must be significantly larger than a single wave length $\lambda \approx 6\lambda_D$ (linear theory predicts $k\lambda_D \approx 1$). To balance the computational costs, we use $L_x \approx 43\lambda_D$ and increase L_y from $22\lambda_D$ up to $43\lambda_D$, depending on the predicted wave angle θ between $\mathbf{v}_{ph}$ and $\mathbf{u}_\alpha$ from linear theory. This also ensures that the spectral resolution is sufficient to determine the wave vector $\mathbf{k}$. Finally, we must choose the number of simulated macro-particles per cell N_{sim}/N_{cell}. To ensure that our simulations deliver physical results, we perform extensive convergence testing. In particular, a sweep over N_{sim}/N_{cell} in one-dimensional simulations reveals that our simulations converge for temperature, wave frequency, and wave number at $N_{sim}/N_{cell} \geq 2^9$. Unfortunately, we were unable to converge on the growth rate of the instability within reasonable computational costs. Our simulations therefore underestimate the growth rate slightly compared to linear theory. A detailed explanation of the convergence testing is provided in Supporting Information S1. In the end, each cell is initialized with 341 macro-particles for each species, respectively. This amounts to roughly 2^{10} particles per cell.

To enable a direct comparison to spacecraft observations, we use plasma parameters taken from the observations by Graham et al. (2025). In particular, the electrons and protons are at rest with $n_e = 12\mathrm{cm}^{-3}$, $n_p = 10\,\mathrm{cm}^{-3}$, $T_e = 100\,\mathrm{eV}$, and $T_p = 3\,\mathrm{eV}$. Whereas the alpha particles have an initial drift velocity of $u_\alpha \in [95, 180]$ km/s in the x-direction with $n_\alpha = 1\,\mathrm{cm}^{-3}$ and $T_\alpha = 12\,\mathrm{eV}$. For reference, these values give $\lambda_D \approx 21.5$ m, a proton plasma frequency $\omega_{pp} = \sqrt{e^2 n_p/(\epsilon_0 m_p)} \approx 4200\,\mathrm{rad/s}$, and proton ion-acoustic speed $c_s = \sqrt{(T_e + 3T_p)/m_p} \approx 102\,\mathrm{km/s}$.

2.2. Geometric Interpretation of Linear Theory

The linear, unmagnetized, electrostatic dispersion relation for the considered Maxwellian plasma is given by (Gary & Omidi, 1987):

$$0 = 1 - \frac{\omega_{pe}^2}{k^2 v_{te}^2}\mathcal{Z}'\left(\frac{\tilde{\omega}}{k v_{te}}\right) - \frac{\omega_{pp}^2}{k^2 v_{tp}^2}\mathcal{Z}'\left(\frac{\tilde{\omega}}{k v_{tp}}\right) - \frac{\omega_{p\alpha}^2}{k^2 v_{t\alpha}^2}\mathcal{Z}'\left(\overbrace{\frac{\tilde{\omega} - k\cos(\theta)u_\alpha}{k v_{t\alpha}}}^{:=-\tilde{\xi}}\right). \tag{1}$$

Here, $\omega_{ps}^2 = q_s^2 n_s/\epsilon_0 m_s$ and $v_{ts}^2 = 2T_s/m_s$ are the plasma frequency and thermal speeds of the plasma species $s \in \{e, p, \alpha\}$, respectively. $\mathcal{Z}'$ is the derivative of the plasma dispersion function (Fried & Conte, 1961), $\tilde{\omega} = \omega + i\gamma$ is the complex frequency, and $\theta \in [0°, 180°]$ is the angle between $\mathbf{k}$ and $\mathbf{u}_\alpha$. Note, however, that waves only grow for $\theta \in [0°, 90°]$, since $\theta > 90°$ corresponds to backward propagating waves.

The influence of u_α on the instability, and subsequently on the plasma heating is the main focus of the present paper. To elucidate the role of u_α in the instability, we define $\xi = \mathrm{Re}\left[\tilde{\xi}\right]$ as the negative real part of the argument of $\mathcal{Z}'$ in the alpha term (third summand) in Equation 1. This yields the following equation:

$$\begin{aligned} \xi(k, \omega, \gamma) &:= \frac{k\cos(\theta)u_\alpha - \omega}{k v_{t\alpha}} \\ \overset{u_\alpha > 0}{\Longleftrightarrow} \cos(\theta) &= \frac{v_{ph} + \xi v_{t\alpha}}{u_\alpha}. \end{aligned} \tag{2}$$

Here, $v_{ph} = \omega/k$ is the phase velocity of the wave. For a wave characterized by a set of k, ω, and γ, the quantity ξ is constant. Note that Equation 2 places an implicit constraint on $u_\alpha \geq v_{ph} + \xi v_{t\alpha}$ through $\cos(\theta) \in [0, 1]$ for growing waves. It follows that as long as u_α fulfills the inequality for a given wave, changing u_α only alters its θ (Gary & Omidi, 1987). If $u_\alpha < v_{ph} + \xi v_{t\alpha}$, then the specified combination of k, ω, and γ no longer solves

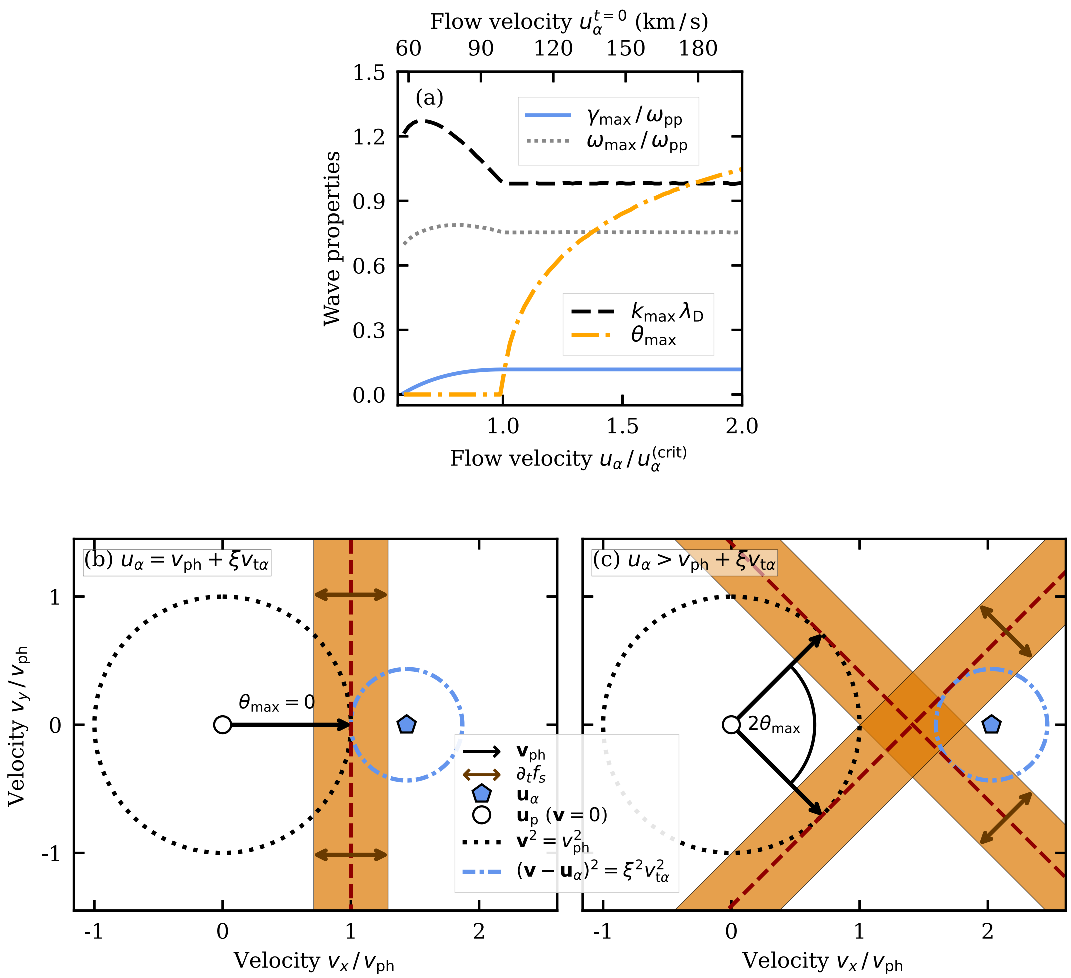

Figure 1. Wave properties and geometric interpretation from linear theory. (a) Wave properties of the most unstable wave as a function of $u_\alpha/u_\alpha^{(crit)}$. Panels (b) and (c) show the particle transport (brown arrows) in the trapping regions (orange intervals) in a two-dimensional cross section of the velocity space (rotational symmetry around $\hat{\mathbf{v}}_x$). The geometry changes between (b) and (c) with the flow velocity u_α (blue pentagon). The centerline (dashed, red) of the interaction region is tangential to two circles: one, centered on origin, characterized by the radius v_{ph} and another centered on u_α of radius $\xi v_{t\alpha}$.

Equation 1. The wave that will dominate in the simulations is the wave of maximum growth-rate. Its wave properties are denoted as k_{max}, ω_{max}, and $\gamma_{max} = \max(\gamma)$, with a corresponding ξ_{max}. The observed wave properties (k_{max}, ω_{max}, and γ_{max}) will only change when $u_\alpha < v_{ph} + \xi_{max} v_{t\alpha} := u_\alpha^{crit}$. We call u_α^{crit} the critical transition velocity. In this regime, $\mathbf{v}_{ph}$ is aligned with $\mathbf{u}_\alpha$, that is, $\theta = 0$.

Figure 1a displays the properties of the most unstable wave as a function of u_α, obtained numerically from Equation 1. In particular, we find $u_\alpha^{crit} \approx 99$ km/s, which is close to the ion sound speed of the electron-proton plasma, $c_s \approx 102$ km/s. Below u_α^{crit}, θ is indeed zero, while ω, k, and γ change. Finally, the growth rate γ reaches zero around $u_\alpha \approx v_{ph}$, and the Landau resonance condition no longer results in wave growth. As explained above, in the $u_\alpha \geq u_\alpha^{crit}$ regime, the wave angle of the most unstable wave increases with u_α, while its other properties remain unchanged. For reference, we find that $\xi_{max} \approx 1.27$.

Another way of understanding the effect that u_α has on the instability is to rewrite Equation 2 as $\hat{\mathbf{k}} \cdot \mathbf{u}_\alpha = v_{ph} + \xi v_{t\alpha}$, where $\hat{\mathbf{k}} = \mathbf{k}/|\mathbf{k}|$. This form is reminiscent of the beam resonance (or Cherenkov resonance) condition $\hat{\mathbf{k}} \cdot \mathbf{u} = v_{ph}$ (Artemyev et al., 2018; Gary & Omidi, 1987), albeit with an additional kinetic correction term $\xi v_{t\alpha}$. In the case of beam resonance, the projection of the beam velocity onto $\mathbf{k}$ equals exactly v_{ph}, while in the present case the projection of $\mathbf{u}_\alpha$ onto $\mathbf{k}$ is larger than v_{ph} by $\xi v_{\mathrm{t}\alpha}$. The role of the $\xi v_{\mathrm{t}\alpha}$ contribution becomes apparent by considering the following: The growth rate due to Landau resonance depends on the velocity gradient of the alpha velocity distribution function (VDF) in the direction of $\mathbf{k}$, $\partial f_\alpha/\partial v_k$ (Fuselier et al., 1987). The ξv_{te} term shifts the Landau resonance velocity from $v_k = \hat{\mathbf{k}} \cdot \mathbf{u}_\alpha$, where $\partial f_\alpha/\partial v_k = 0$ for Maxwellians (yielding no wave growth), to $v_k = \hat{\mathbf{k}} \cdot \mathbf{u}_\alpha - \xi v_{\mathrm{te}}$, where, for $\xi > 0$, $\partial f_\alpha/\partial v_k > 0$, thereby enabling wave growth.

The impact of u_α on the geometry of the instability and, subsequently, on the heating, can be visualized through the velocity space diagrams shown in Figures 1b and 1c, similar to Figure 3 in Fuselier et al. (1987). The centers of the initial proton and alpha distributions, that is, $\mathbf{u}_{\mathrm{p}}$ and $\mathbf{u}_\alpha$, are marked by the white circle and blue pentagon, respectively. The phase velocity v_{ph} of a given wave (characterized by k, ω, γ, ξ) traces a circle (black, dotted) around the origin in velocity space. Similarly, the $\xi v_{t\alpha}$-term traces out a circle around $\mathbf{u}_\alpha$ (blue, dash-dotted) of radius $\xi v_{t\alpha}$. The Landau resonance condition in an unmagnetized plasma reads $\mathbf{v} \cdot \hat{\mathbf{k}} = v_{\mathrm{ph}}$, and is represented by a straight line that is tangential to the circle from $\mathbf{v}_{\mathrm{ph}}$ (red, dashed line). It follows from the previous discussion that, for some given values of v_{ph}, u_α, and ξ, the angle θ obtained from Equation 2 is the one that makes the Landau resonance line tangential to both the v_{ph} and $\xi v_{t\alpha}$ circles. Since the problem is symmetric with respect to the x-axis, there are two such lines when $\theta > 0$, corresponding to solutions with $\pm k_y$ (in 3-dimensions this picture is cylindrically symmetric, and the resonance lines trace out a cone). In the interaction range (orange area), particles are transported back and forth in the direction of $\mathbf{k}$ by the electric field. The extent of this transport is bounded by the trapping velocity $v_{\mathrm{trap}}^2 = 2q_s\phi/m_s$, where ϕ is the wave electric potential. The difference between Figures 1b and 1c illustrates how changes in u_α affect the rotation of this interaction range (i.e., θ) and therefore the particle transport. As u_α increases θ must increase for the resonance line to remain tangential to both circles, with $\lim_{u_\alpha \to \infty} \theta = 90°$. This graphical interpretation also clearly shows that v_{ph} and/or $\xi v_{t\alpha}$ must decrease for $u_\alpha < u_\alpha^{\mathrm{crit}}$; otherwise, a growing wave symbolized by the tangent line cannot exist.

3. Results

3.1. Temporal Evolution

The evolution of the instability is illustrated in Figure 2 for $u_\alpha = 95\ \mathrm{km/s} < u_\alpha^{\mathrm{crit}}$ (panel (a) and blue curves) and $u_\alpha = 140\ \mathrm{km/s} > u_\alpha^{\mathrm{crit}}$ (panel (b) and black curves). Figure 2c displays the mean electric field energy over time. All simulations consist of three phases: For $t\omega_{\mathrm{pp}} < 20$, any coherent spatial variations are below the noise floor which is set by the number of macro-particles. This means that the electric fields are small. All particle species remain close to their initial temperatures $T_s^{t=0}$. Next, the instability transitions to the linear regime ($45 < t\omega_{\mathrm{pp}} < 55$). Here, the total electric field energy grows exponentially along with the species temperatures (Figures 2c–2f) at the expense of the bulk kinetic energy of the alpha particles. Finally, the plasma enters a nonlinear regime beyond $t\omega_{\mathrm{pp}} \approx 55$. The electric field energy in Figure 2c plateaus and subsequently slowly decays. During this phase the previously (mostly) planar wave breaks up into nonlinear structures, and ion phase space holes form. The heating rate slows down until it approaches zero.

For all simulated velocities u_α, the wave amplitudes reach several 100 mV/m, comparable to observations (Graham et al., 2025). The waves are electrostatic; hence, the direction of $\mathbf{k}$ sets the direction of $\mathbf{E}$ via $\mathbf{E} \times \mathbf{k} = 0$. For $u_\alpha = 95\ \mathrm{km/s}$, linear theory predicts $\theta_{\max} = 0$, that is, $k_{\max} = k_x$. Indeed, Figure 2c shows wave fronts in the x-direction, that is, $k_x \gg k_y$. Due to the strong E_x, the ion heating is also dominated by T_x (black dashed lines in d-f). This gives rise to a strong temperature anisotropy by the end of the simulation, where $\Delta T_x/\Delta T_y \approx 2$. In contrast, when $u_\alpha = 140\ \mathrm{km/s}$ we find a typical interference pattern due to $k_y \approx \pm k_x$. In this case, $E_x \approx E_y$, and the plasma is heated to a similar extent in both x and y directions.

Over the course of the instability, the alpha population loses a significant fraction (33%–45%) of its initial kinetic energy density, $K_\alpha^{t=0} = m_\alpha n_\alpha \left(u_\alpha^{t=0}\right)^2/2$. Roughly 95% of the lost energy is converted into plasma heating. Of the remaining 5%, most is converted to proton bulk kinetic energy. The increase of proton and alpha thermal energy density ($\Delta U_{\mathrm{s}} = (3/2) n_{\mathrm{s}} \Delta T_{\mathrm{s}}$) equates to roughly 67% and 26% of the lost K_α, respectively. In Figures 2d–2f, we show how this heating affects the two components of the particle temperatures, T_x and T_y. For the simulation at $u_\alpha^{t=0} = 95\ \mathrm{km/s}$ (black lines), the protons are mainly heated in the x-direction, with $T_{\mathrm{p}x}$ reaching almost 10 eV (roughly a factor 3 increase). On the other hand, $T_{\mathrm{p}y}$ stays below 5 eV (roughly a factor 1.6 increase). The alpha

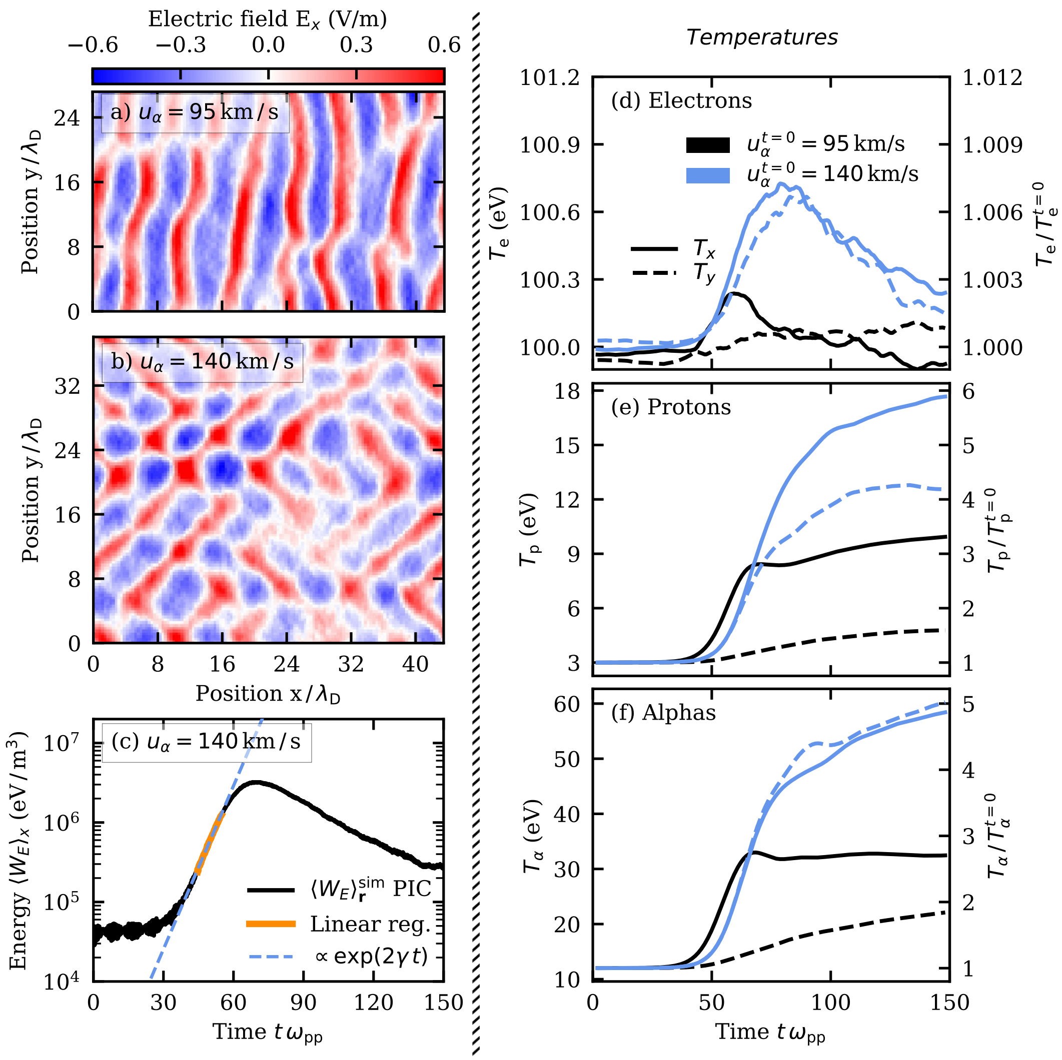

Figure 2. Temporal evolution of the instability for $u_\alpha = 95$km/s and $u_\alpha = 140$km/s (a–b) Spatial distribution of E_x in the two simulations near the end of the linear stage of the instability at $t\omega_{pp} = 55$. (c) Evolution of the electric field energy density in the $u_\alpha = 140$km/s simulation. The orange interval indicates the linear regime of the instability. The right column (d–f) shows the temporal evolution of T_x (solid) and T_y (dashed) for $u_\alpha = 95$km/s (black) and $u_\alpha = 140$km/s (blue) averaged over space. The left y-axes show the temperatures in eV, and the right y-axes show the temperatures normalized to the corresponding initial value.

particle temperature increases by similar factors, with $T_{\alpha x}$ and $T_{\alpha y}$ reaching approximately 32 eV and 22 eV, respectively.

Note that the velocities in our simulations are three-dimensional. However, because the system only has two spatial degrees of freedom, the instability cannot develop in the z-direction, and T_z remains unchanged for all species. As a result, the total temperature $T = (T_x + T_y + T_z)/3$ likely deviates from the total temperature obtained in the corresponding 3D system. In our case, we find that T_p and T_α reach roughly 6 and 22 eV, in the $u_\alpha^{t=0} = 95$ km/s case. For the simulation at $u_\alpha^{t=0} = 140$ km/s (blue lines), the oblique wave fronts result in a more balanced heating between the components. Here, the alpha-particles reach $T_{\alpha x} \approx T_{\alpha y} \approx 60$ eV, corresponding to an increase of a factor 5. The protons are still preferentially heated in T_{px}, which reaches 18 eV while T_{py} reaches 13 eV. The total temperatures for protons and alphas in this simulation reach roughly 11 and 43 eV.

Figure 2d shows that the instability has a very minor effect on the electron population, which gains less than 1 eV (<1%) in both simulations. This can be explained as follows: The resonant interaction between the wave and the

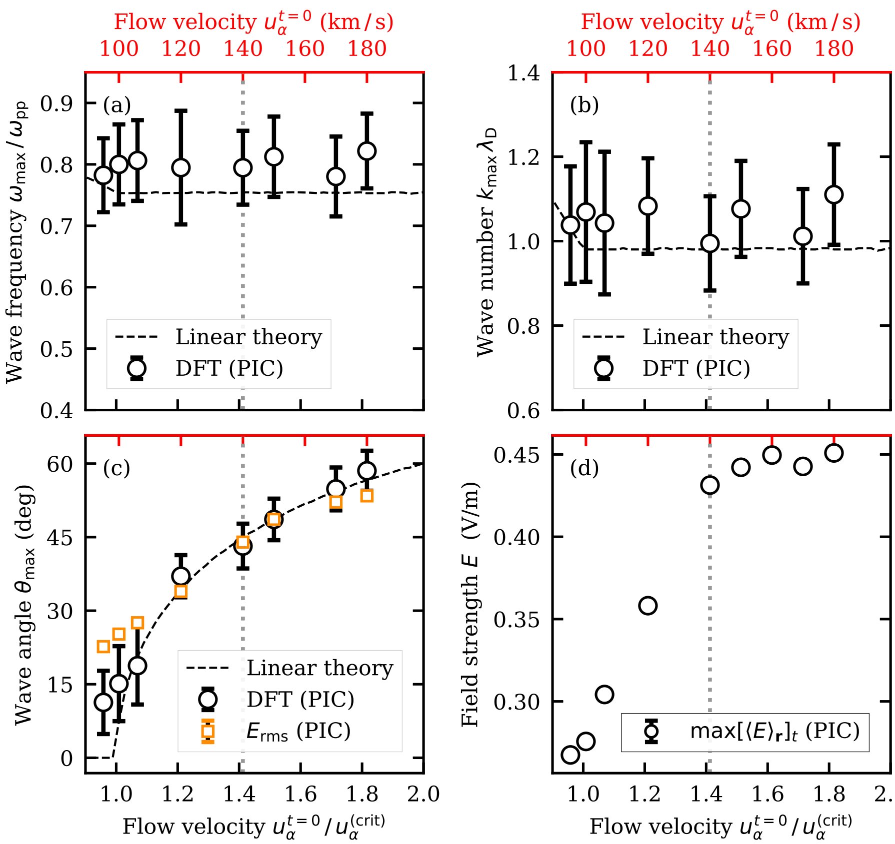

Figure 3. Wave properties for different values of u_α in normalized and absolute units (black and red x-axis, respectively): (a) Wave frequency estimate via the discrete Fourier transform (DFT) applied to the linear regime (black circles), and the prediction of the fastest growing mode in linear theory (dashed line). The error bars show both the combined uncertainty due to the spectral resolution and the subgrid estimation. (b) Same as (a) but for wavenumber. (c) Wave angle estimated using DFT (black circles) and Faraday's law (orange boxes), and the linear theory prediction. (d) Spatially averaged, maximum electric field strength from the simulation. For the θ estimate via E_{rms} in (c) and electric field strengths in (d), the statistical error is below symbol size and thus not visible. The vertical dotted lines mark $u_\alpha^{t=0} = 140$ km/s ($\theta \approx 45°$).

electrons is restricted to low speed electrons ($v_{\mathrm{ph}} \ll v_{\mathrm{te}}$). In this regime, the gradient of the electron VDF $\nabla_v f_{\mathrm{e}}$ is small and the resonant diffusion due to the instability has a very small effect on the temperature. Therefore, we will not discuss the effect of the instability on the electrons further.

3.2. Wave Properties

For all runs, we compute the (angular) wave frequency $\omega_{\max}$ and wave number $\mathbf{k}_{\max}$ of the dominant wave mode. In particular, we find the wave with maximum power using a discrete Fourier transform (DFT) over the two-dimensional electric field in all time steps before the end of the linear regime. Finally, we perform a localized quadratic fit for subgrid estimation of $\omega_{\max}$ and $\mathbf{k}_{\max}$. For the estimate of the wave angle $\theta_{\max}$, we use two different methods: The first relies on the wave vector (k_x, k_y) from the Fourier analysis. It gives the wave angle via $\theta = \arctan(|k_y|/|k_x|)$. The second relies on Faraday's law, which, for electrostatic waves, gives $\mathbf{E} \times \mathbf{k} = 0$. Consequently, $\mathbf{E}$ and $\mathbf{k}$ are coaxial vectors. This means we obtain an estimate directly from $\mathbf{E}^{\mathrm{rms}}$: $\theta = \arctan\left(|E_y^{\mathrm{rms}}|/|E_x^{\mathrm{rms}}|\right)$.

Figure 3 compares our simulation results with the properties of the most unstable mode predicted by linear theory (cf. Equation 1); overall, they are in good agreement. The frequency is $\omega \approx 0.8\omega_{\mathrm{pp}} \approx 3.1 \cdot 10^3$ rad/s the wavenumber $k \approx 1.0/\lambda_{\mathrm{D}} \approx 0.046$/m, and the corresponding phase velocity $v_{\mathrm{ph}} \approx 0.7c_{\mathrm{s}} \approx 69$ km/s. We primarily attribute the observed deviations from linear theory to two independent effects:

First, the grid resolution and output frequency of the PIC simulations determine the resolution in Fourier space (ω, k_x, k_y). At our settings, the spacing between possible values is $\Delta\omega/\omega_{\mathrm{pp}} \approx 0.1$ and $\Delta k\lambda_{\mathrm{D}} \approx 0.15$. This fundamentally limits the number of observable and allowed wave modes in the simulation. The systematic bias in Figure 3a and 3b is most likely a symptom of the limited k-space resolution.

Second, in the simulations, several wave modes grow in a broadly peaked distribution. This reflects the fact that the growth rate has a broad peak in linear theory (Graham et al., 2025). Thus, the wave spectra in our simulations need not have a sharp peak centered on the mode of maximum growth rate. Instead, the small initial spatial perturbations persist throughout the growth phase and determine the strength of different wave modes. Figure 3c clearly shows that both estimation methods for θ deviate more from the theory for shallow wave angles. In these runs, numerical noise introduce wave modes with $E_y > 0$, and thus $k_y > 0$, which grow over time. As a result, we measure $\mathbf{k}$ and thus θ with large uncertainties. Toward larger θ, the bias due to such artifacts is reduced as the uncertainty becomes symmetric $\Delta k_x \approx \Delta k_y$. The impact of the broad range of wave modes also affects the electric field in Figure 2a, where the phase fronts are not perfectly straight.

Finally, Figure 3d shows the maximum of the spatially averaged wave amplitude $|\mathbf{E}|$ as a function of u_α in the simulations; the linear theory via Equation 1 makes no predictions. For reference, the simulations with an average of 0.45 V/m have waves with peak amplitudes up to around 1.5 V/m. We observe that the average wave amplitude strongly increases up to $u_\alpha^{t=0} \approx 140$ km/s. For higher u_α, this increase is much slower. The transition occurs around $u_\alpha^{t=0} = 140\,\mathrm{km/s}$, where the two bands of the Landau interaction range, and thus the corresponding electrostatic waves, are orthogonal ($\theta \approx 45°$, cf. Figure 1c).

3.3. Plasma Heating

While ω, k, and consequently the phase speed $v_{\mathrm{ph}} = \omega/k$ are constant within our uncertainty, θ and $|E|$ are not. This is in agreement with linear theory (cf. Figure 1). Consequently, we find that the instability affects the plasma differently, on both a fluid and kinetic level, for different values of u_α. On a fluid level, we quantify this effect as the change in temperature ΔT_s of the particle species s. Figure 4 displays the temperature changes for the two ion species. Clearly, both are subject to a strong interaction and experience significant heating.

As we increase u_α from the subcritical 95 km/s, the proton temperature increases by about 1.0–3.2 $T_p^{t=0}$, corresponding to 4–10 eV, depending on u_α (Figure 4a). This is large compared to the initial $T_p = 3$ eV. Similarly, we find that T_α increases by about $0.8 - 3.8\,T_\alpha^{t=0}$ (Figure 4b), corresponding to 10–45 eV which, again, is large compared to the initial $T_\alpha = 12$ eV. The fact that the ions gain more energy for increasing u_α is not surprising; a larger u_α implies additional free energy in the system that can be converted to heat. As such, we expect the heating to increase indefinitely with higher u_α.

To see when the instability is most efficient at heating the plasma relative to the energy input, we normalize the change of thermal energy density, ΔU_s, to $K_\alpha^{t=0}$. These results are presented in the bottom row of Figure 4. Among our simulations, the $u_\alpha^{t=0} = 140\,\mathrm{km/s}$ case, which corresponds to $\theta \approx 45°$ (marked by the vertical dotted line), shows the highest heating efficiency. Here, up to 30% and 11% of the available flow energy density is converted into proton and alpha thermal energy density, respectively. This geometry is favorable because the orthogonal bands have minimal overlap and the waves can extract energy from the alphas efficiently. Toward even higher flow velocities, following the same logic, the wave angle is less ideal. However, at the same time, a larger u_α increases the free energy in the system which results in more wave growth and a wider interaction range. Thus, both the heating and the electric field strength still increase with u_α but with a reduced rate (cf. Figures 3d and 4a and 4b). In line with this reasoning, Figure 4c and d show that as u_α increases beyond 140 km/s, the heating efficiency decreases.

To develop an understanding of why the heating is most efficient for $\theta = 45°$, we turn to the kinetic aspects of the instability. This helps clarify how the distribution functions are modified, and how individual particles transfer energy to the waves.

3.4. Wave-Particle Interactions and VDF Evolution

Here, we compare the geometric considerations in Section 2.2 with our simulations. In the PIC-simulations, we can directly measure the full VDFs of all particle species. Figure 5 displays the VDFs of alphas and protons for

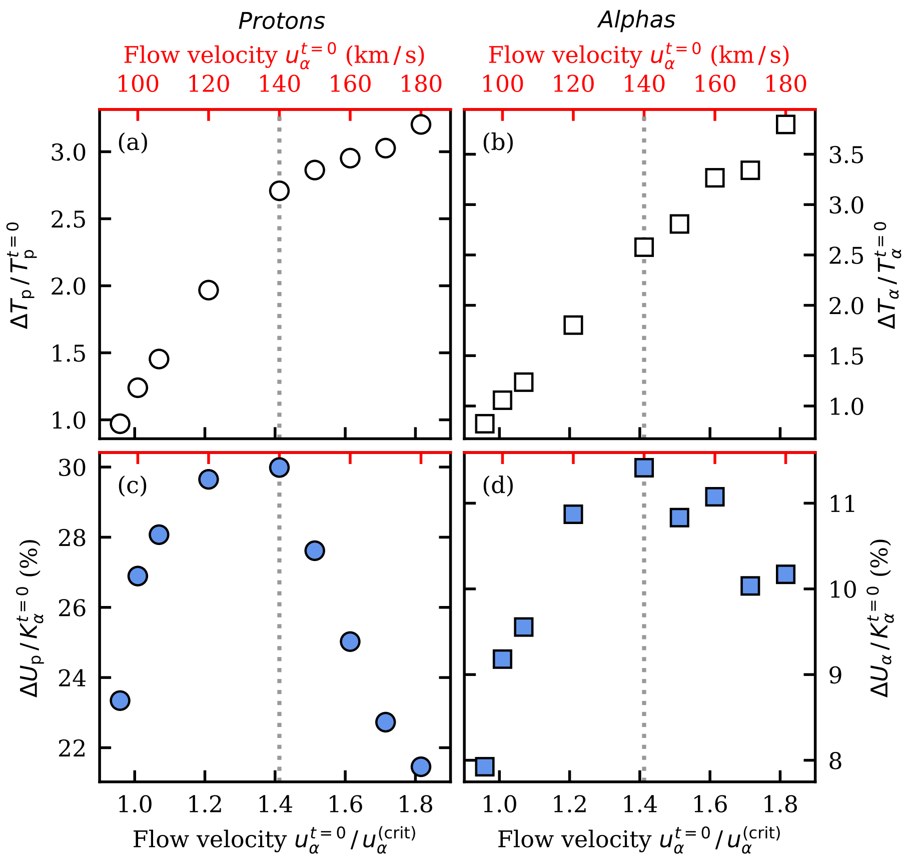

Figure 4. Changes in temperature (a–b) and thermal energy density (c–d) of the protons and alpha species as a function of u_α. The temperature difference is taken between the first and last timestep of the simulation. Normalization is performed with respect to the initial species temperature (a–b) or the initial kinetic energy density of the alphas $K_\alpha^{t=0}$ (c–d). The vertical dotted lines mark $u_\alpha^{t=0} = 140$ km/s ($\theta \approx 45°$).

$u_\alpha^{t=0} = 95$ km/s and $u_\alpha^{t=0} = 140$ km/s, which makes them directly comparable to Figures 1b and 1c. The transparent bands in Figure 5 indicate the interaction range. Their angle to the x-axis is determined by the wave angle $\theta_{\max}$, which we obtain numerically from Equation 1. In order to compute the interaction width v_{trap}, we use the 99.9th percentile of the electric potential ϕ from the respective simulation up to the displayed time step. The black arrows indicate the direction of transport in the respective band. In their overlap region, particles are transported in both directions. The full evolution of the VDFs for all three species for three values of $u_\alpha^{t=0}$ can be seen in Movie S1 in the supporting information.

Initially, the VDFs of all particle species are Maxwellian and the width of the interaction range is set by the noise level. As the instability evolves, the resonant alpha particles are, on average, giving energy to the wave. In contrast, the resonant protons are, on average, taking energy from the wave. The net effect is a growing wave, that is, an increasing interaction range, which in turn increases the amount of resonant particles, enabling further wave-growth. This avalanche effect is what characterizes the linear growth phase of the instability. Figure 5a, 5b and 5d, and 5e show the VDFs near the end of the linear growth phase of the instability ($t\omega_{\mathrm{pp}} = 55$). Here, we find an excellent agreement between each VDF and its interaction bands with respect to both the direction and the extent of the particle transport. There is little to no change in the phase space density outside the interaction range. One important qualitative difference between the $\theta = 0°$ (Figures 5a and 5d) and $\theta = 45°$ (Figure 5b vs. e) scenarios is the following: In the latter, the instability results in two waves (with $k_y \approx \pm k_x$) and thus two interaction bands. Specifically for Figure 5b in contrast to Figure 5e, the overlap of these two bands is located in a region where the phase-space density is non-zero. Particles in this overlap resonate with both waves simultaneously. Consequently, these particles are transported in both directions, eventually filling the overlap region (cf.

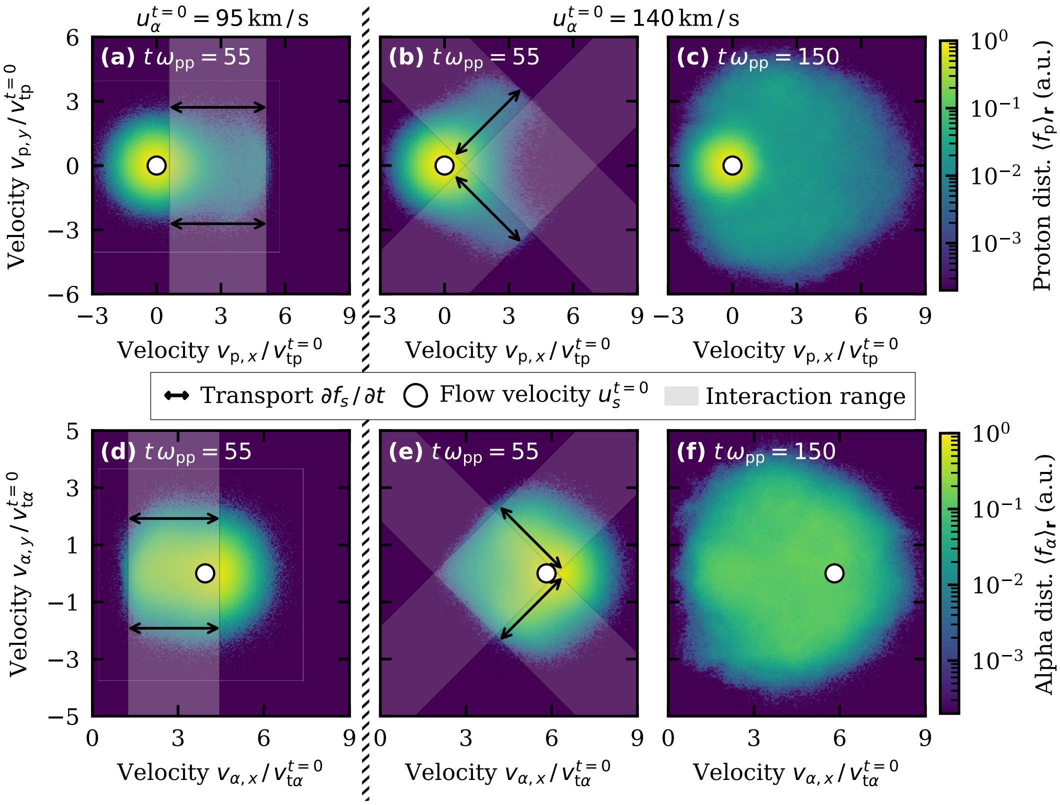

Figure 5. The velocity distribution functions (VDFs) of protons and alpha particles. They are normalized such that the phase space density reaches its maximum at 1 over the entire simulation period. The transparent bands indicate the interaction range of the Landau resonance and the black double arrows give the predicted direction of particle transport. The simulations with $u_\alpha^{t=0} = 95$ km/s and $u_\alpha^{t=0} = 140$ km/s are compared near the end of the linear regime at $t\omega_{pp} = 55$ in panels (a), (b), (d), and (e). Panels (c) and (f) display the VDFs in the non-linear regime at $t\omega_{pp} = 150$. See Movie S1 in the supporting information for the complete VDF evolution.

Figure 5e). The combined interaction displaces the resonant particles further in phase-space than they would have been without this effect, resulting in additional heating.

Eventually, the instability enters the non-linear regime (after $t\omega_{pp} \approx 55$); the wave amplitude saturates and then gradually declines (cf. Figure 2). Finally, at the end of the simulation ($t\omega_{pp} = 150$), the VDFs of both ion species are characterized by wide plateaus (Figures 5c and 5f). While some structured features associated with the interaction bands are still present, the VDFs generally become more well mixed. This is likely due to the presence of nonlinear waves: First, the wave fronts are non-planar. Hence, the direction of the electric field, which determines the direction of the particle transport, varies more broadly. Second, we observe localized spots with very high electric field strength. These create a strong electric potential and consequently wide interaction range via v_{trap}. Both of these features can scatter the particles, thereby contributing to the observed mixing. The proton VDF retains a distinct peak around $u_p^{t=0}$ (cf. Figure 5f), while the alpha VDF flattens out completely (cf. Figure 5f).

These VDFs in the late stage of the instability are a result of the location and width of its interaction range. At its closest point during the linear regime, the center of the interaction range is at least $\xi v_{t\alpha} \approx 1.27 v_{t\alpha}$ from the core alpha distribution $\left(\mathbf{u}_\alpha^{t=0}\right)$. Its one-sided width (i.e., the trapping velocity) is $v_{trap} \approx v_{t\alpha}$. Therefore, the interaction range covers almost the entire core of the alpha VDF (cf. Figure 5e). For the protons, the trapping velocity grows to $v_{trap} \approx 2.17 v_{tp}$, due its dependence on species mass. In the linear regime, the interaction range never reaches the proton core $\left(u_p^{t=0}\right)$, with a center-to-core distance of $v_{ph} \approx 2.86 v_{tp}$. Although nonlinear fields occasionally increase the interaction width, the proton core will be rarely affected. Thus, it barely changes over the course of the simulation (cf. Figure 5c). Finally, we remark that the VDFs in Figure 5 are mirror symmetric about the x-axis.

More generally, streaming instabilities in 3D space that start from a Maxwellian and have a single streaming component are cylindrically symmetric around the streaming velocity (here $\mathbf{u}_\alpha^{t=0}$).

The Landau resonance broadens the VDF in the direction of the phase velocity. This directly corresponds to a temperature increase in that direction. We observe this in Figures 2e and 2f. For $u_\alpha^{t=0} = 95$ km/s, the temperature predominantly increase in the x-direction ($\Delta T_x \gg \Delta T_y$). Then, for $u_\alpha^{t=0} = 140$ km/s, the heating in the y-direction increases significantly ($\Delta T_x \approx \Delta T_y$). Importantly, for a 45° wave angle, the two bands of the interaction range are orthogonal. This minimizes their overlap in phase space, which in turn maximizes the heating efficiency (cf. Figure 4).

4. Discussion

In this section, we discuss the applicability and limitations of our approach and the presented simulations.

The density ratio $n_\alpha/n_\mathrm{p} = 0.1$ is kept fixed in this study. Nevertheless, we can still reason about its effect on the instability through the connected energies. Increasing n_α/n_p, while keeping the total charge constant, implies the number of alpha particles increases. Through the alpha flow velocity, this increases the available kinetic energy in the system. In this regime of large n_α/n_p, the linear theory predicts high growth rates (cf. Figure 4h in Graham et al. (2025)) and we expect a more rapid thermalization. In all simulations, the strength of the initial electric fields is set by the discretization noise and thus the number of macro-particles. As such, for larger values of n_α/n_p, a larger number of macro-particles are required to counteract an increased sensitivity to the initial perturbations. For small n_α/n_p, we must resolve the weak wave growth compared to discretization noise, again necessitating an increased number of macro-particles to reduce the noise.

We have neglected the effect of background magnetic fields in our simulations. Generally, the magnetic field strength near the Earth's bow shock and in the magnetosheath is on the order of several tens of nanotesla, and the density is on the order of several tens of particles per cubic centimeter. This gives a proton plasma-to-cyclotron frequency ratio on the order of 1,000. However, the instability saturates over less than 100 ω_pp^{-1}; the gyration of the ions is much slower than the timescales of the instability and the ions thus behave as effectively unmagnetized. In fact, at a magnetic field strength of $B = 45$nT (cf. shocks in Graham et al. (2025)), the protons and the alpha particles gyrate less than 60° and 30° over the entire simulation period (150 ω_pp^{-1}). We remark that the electrons are magnetized at such plasma parameters and timescales, but their effect on the instability is expected to remain negligible.

Our simulations made use of plasma parameters relevant for Earth's bow shock, but they were otherwise isolated from the collisionless shock context. Here, we will put our results back into context, and understand in which regions of the Earth's bow shock (or any similar shock) we expect our results to be relevant. The energy source of the instability is the relative drift, u_α, between protons and alphas. Such u_α can be, but for the purpose of the instability need not be, a consequence of the differential acceleration by the cross-shock potential (e.g., Gedalin, 2020; Gedalin et al., 2023; Graham et al., 2025; Madanian et al., 2024). In the case of Graham et al. (2025), significant $u_\alpha \approx 200$ km/s was found to develop in the shock-front and persist far (100s of km, corresponding to several proton inertial lengths, $d_\mathrm{p} = c/\omega_\mathrm{pp}$) downstream. We should thus expect that the instability can be active from near the shock front, where u_α starts developing due to the cross-shock potential, to several d_i downstream. Indeed, Graham et al. (2025) reported observations of ion-acoustic waves throughout the interval of large u_α. Because the ions are effectively unmagnetized during the time scales of the instability, the axis of symmetry of the system is set by $\mathbf{u}_\alpha$. Close to the shock ramp, the cross-shock potential yields $\mathbf{u}_\alpha \approx u_\alpha \hat{n}$, where $\hat{n}$ denotes the shock normal direction, for both quasi-parallel and quasi-perpendicular shocks. Further downstream, for quasi-perpendicular shocks, the gyro motion gives $\mathbf{u}_\alpha$ a component tangential to the shock front as well. An alternative mechanism to generate a relative proton-alpha drift is shock reflection. In that case, however, the dynamics will likely be dominated by proton-proton instabilities driven by the interaction between the reflected and incoming protons (e.g., Fuselier et al., 1987; Goodrich et al., 2019; Vasko et al., 2022). Differential proton-alpha flows up to the local Alfvén speed are commonly observed parallel to the magnetic field in the solar wind, even in the absence of shocks (Mostafavi et al., 2022; Steinberg et al., 1996). Because the solar wind Alfvén speed can exceed the ion-acoustic speed, so can these differential flows, potentially triggering the proton-alpha instability. Our results might therefore also be applicable to the solar wind, particularly close to the sun, where the speed differential tends to be largest (Mostafavi et al., 2022).

Another constraint on the applicability of our results is the use of periodic boundary conditions and an initially homogeneous plasma. This choice of boundary conditions gives the instability a fully isolated domain in which it may develop. In reality, however, the plasma surrounding collisionless shocks tend to be subject to strong spatiotemporal variations and turbulence. Our model is therefore only applicable in regions where the use of periodic boundary conditions is justified. To quantify the scales over which this choice is justified, we estimate the travel distance of the plasma until the end of the growth phase. Taking a generous average bulk velocity of 300 km/s, and a time span of 100 $\omega_{\mathrm{pp}}^{-1}$, we find that the plasma has time to traverse approximately 0.1 d_{p}. This is generally a short distance with respect to Earth's ion-scaled bow shock (e.g., Bale et al., 2003; Greenstadt et al., 1975), showing that the homogeneous and periodic model is representative unless strong gradients on sub-ion scales are present. We stress, however, that this is a constraint related to our numerical model, and it does not imply that the instability should necessarily be suppressed at sub-ion scale shocks.

As the observational VDFs have very low resolution, it is difficult to determine to what extent the assumption of initially Maxwellian velocity distributions is justified. In fact, it is likely that they are not exactly Maxwellian (e.g., Graham et al., 2024; Kucharek et al., 2004). However, since the alpha particles are initially very cold $\left(v_{\mathrm{t}\alpha} \ll u_\alpha^{(t=0)}\right)$ and the instability eventually thermalizes the entire alpha distribution (Figures 5e and 5f) we expect minor deviations from Maxwellianity to have a negligible effect on the instability.

Our results show that the ion heating increases with u_α and consequently θ (Figure 4). Since u_α here is the relative drift between protons and alpha particles, it is proportional to the square root of the cross-shock potential (Graham et al., 2025). In-situ investigations of Earth's bow shock have shown that the cross-shock potential is highly variable and only weakly correlated with Alfvénic Mach number (M_{A}) and shock-normal angle (θ_{Bn}) (Dimmock et al., 2012). This suggests that the proton-alpha streaming instability can be an important dissipation mechanism for Earth's bow shock over a large range of M_{A} and θ_{Bn}. However, there is a tendency for the cross-shock potential to decrease with increasing M_{A} (Dimmock et al., 2012) and to reach higher values for increasing θ_{Bn}. The instability might therefore be particularly important for more perpendicular, low M_{A} shocks.

5. Conclusions

In the present paper, we have studied the proton-alpha streaming instability in PIC simulations to further our understanding of plasma heating at collisionless shocks. In particular, we have investigated how the electrons, protons, and alpha particles are heated as a function of the initial alpha flow velocity u_α, on a fluid and kinetic level. In addition, we have developed a geometrical interpretation of the instability in velocity space, which provides us with insights into how the instability heats the plasma on a kinetic level (see Figures 1 and 5).

Our simulations show that the instability generates electrostatic waves with peak amplitudes at and above 1 V/m. The waves have wavelengths comparable to the Debye length, with frequencies below the proton plasma frequency, and phase speeds below the proton ion-acoustic speed. These properties are consistent with spacecraft observations (Graham et al., 2025). Up to the end of the linear growth phase, the wave properties in the simulations are consistent with numerical solutions of the dispersion relation from linear theory (cf. Figure 3). At later times, linear theory is no longer applicable, the wavefronts become non-planar, and ion phase space holes are formed.

The PIC simulations capture the fully non-linear evolution of the velocity distribution function (VDF) of all species. From these, we find that the instability is a significant source of ion heating. At $u_\alpha^{t=0} = 95\mathrm{km/s}$ (for reference $c_{\mathrm{s}} \approx 102\mathrm{km/s}$), $\mathbf{k}$ is parallel to $\mathbf{u}_\alpha^{t=0}$. Here, the temperatures of both the proton and the alpha population increase by approximately a factor of two. At $u_\alpha^{t=0} \approx 140\mathrm{km/s}$, the angle between $\mathbf{k}$ and $\mathbf{u}_\alpha^{t=0}$, denoted θ, is about 45°. In this configuration, the largest fraction of the initial kinetic energy density of the alpha particles is converted to proton and alpha thermal energy, 30% and 11%, respectively (cf. Figures 4 and 5). The proton and alpha temperatures increase by almost a factor of five. Generally, the instability has a negligible effect on the electrons, whose temperature changes are on the order of 1%.

In order to understand how the instability heats the plasma on a kinetic level, we formulate a geometric interpretation of the instability. This interpretation provides an intuitive explanation of how the wave angle θ of the most unstable wave changes with $u_\alpha^{t=0}$. Moreover, it correctly describes how the Landau resonance reshapes the VDFs (cf. Figures 1 and 5). Finally, it provides an intuitive explanation for why the most efficient heating occurs at $\theta = 45°$.

Our model assumes the presence of a relative drift ($\mathbf{u}_\alpha$) between protons and alpha particles. In nature, such a drift has been observed from the shock ramp to several d_p downstream as a consequence of the cross-shock potential (Graham et al., 2025). We therefore expect the instability to be active in this wide region. Alpha-proton drifts have also been observed in the solar wind (Mostafavi et al., 2022; Steinberg et al., 1996), providing another environment where the instability may be important.

While this work has provided new insights into the proton-alpha instability in the context of Earth's bow shock, unanswered questions remain. For example, how does the relevance of the proton-alpha instability depend on shock parameters and upstream conditions, and how does it compete with other instabilities in physical shocks, where turbulence and other processes are active? Since the relative drift can be a direct consequence of the cross-shock potential, expanding on the in-situ cross-shock potential statistics of Dimmock et al. (2012) together with hybrid simulations (e.g., Gedalin et al., 2023; Madanian et al., 2024) could prove fruitful for understanding under what conditions a significant differential flow of ions is expected to develop. Due to instrument limitations on past and contemporary spacecraft missions, it is currently difficult to accurately determine the wave properties and study the structure and evolution of the distribution functions in-situ (Goodrich et al., 2023). Local PIC simulations of shocks could therefore be an important complement, contributing to furthering our understanding of the development of this instability in a more realistic setting.

Conflict of Interest

The authors declare no conflicts of interest relevant to this study.

Availability Statement

All simulation data, input files, and code used to produce this manuscript are available at Müller et al. (2026). The code is additionally available in a GitHub-repository at https://github.com/insalt-glitch/proton-alpha-instability-simulations. To produce the simulation results we used the EPOCH commit v4.19.5-4-g05c1ef21-clean, that is, the tagged version 4.19.5 (git versioning-system).

Acknowledgments

We are grateful to Lise Hanebring and Tünde Fülöp for valuable discussions. This project received funding from the Knut and Alice Wallenberg Foundation (Grant KAW 2022.0087 and 2023.0249), and the Swedish Research Council (Dnr. 2021-03943). The computations and data handling were enabled by resources provided by the National Academic Infrastructure for Supercomputing in Sweden (NAISS), partially funded by the Swedish Research Council through Grant 2022-06725. The EPOCH code used in this work was in part funded by the UK EPSRC Grants EP/G054950/1, EP/G056803/1, EP/G055165/1, EP/M022463/1 and EP/P02212X/1.

References

Arber, T. D., Bennett, K., Brady, C. S., Lawrence-Douglas, A., Ramsay, M. G., Sircombe, N. J., et al. (2015). Contemporary particle-in-cell approach to laser-plasma modelling. *Plasma Physics and Controlled Fusion*, *57*(11), 113001. https://doi.org/10.1088/0741-3335/57/11/113001

Arber, T. D., Bennett, K., Brady, C. S., Lawrence-Douglas, A., Ramsay, M. G., Sircombe, N. J., et al. (2024). EPOCH commit v4.19.5-4-g05c1ef21-clean. Retrieved from https://github.com/epochpic/epoch/tree/v4.19.5

Artemyev, A., Neishtadt, A., Vainchtein, D., Vasiliev, A., Vasko, I., & Zelenyi, L. (2018). Trapping (capture) into resonance and scattering on resonance: Summary of results for space plasma systems. *Communications in Nonlinear Science and Numerical Simulation*, *65*, 111–160. https://doi.org/10.1016/j.cnsns.2018.05.004

Bale, S. D., Mozer, F. S., & Horbury, T. S. (2003). Density-transition scale at quasiperpendicular collisionless shocks. *Physical Review Letters*, *91*(26), 265004. https://doi.org/10.1103/PhysRevLett.91.265004

Balikhin, M., Walker, S., Treumann, R., Alleyne, H., Krasnoselskikh, V., Gedalin, M., et al. (2005). Ion sound wave packets at the quasi-perpendicular shock front. *Geophysical Research Letters*, *32*(24), 2005GL024660. https://doi.org/10.1029/2005GL024660

Baumjohann, W., & Treumann, R. A. (2012). *Basic space plasma physics* (Revised ed.). World Scientific Publishing Company.

Boldú, J. J., Graham, D. B., Morooka, M., André, M., Khotyaintsev, Y. V., Dimmock, A., et al. (2024). Ion-acoustic waves associated with interplanetary shocks. *Geophysical Research Letters*, *51*(16), e2024GL109956. https://doi.org/10.1029/2024GL109956

Burch, J. L., Moore, T. E., Torbert, R. B., & Giles, B. L. (2016). Magnetospheric multiscale overview and science objectives. *Space Science Reviews*, *199*(1), 5–21. https://doi.org/10.1007/s11214-015-0164-9

Burgess, D., & Scholer, M. (2015). *Collisionless shocks in space plasmas: Structure and accelerated particles*. Cambridge University Press.

Cairns, I. H., Knock, S. A., Robinson, P. A., & Kuncic, Z. (2003). Type II solar radio bursts: Theory and space weather implications. *Space Science Reviews*, *107*(1), 27–34. https://doi.org/10.1023/A:1025503201687

Cairns, I. H., Robinson, P. A., Anderson, R. R., & Strangeway, R. J. (1997). Foreshock langmuir waves for unusually constant solar wind conditions: Data and implications for foreshock structure. *Journal of Geophysical Research*, *102*(A11), 24249–24264. https://doi.org/10.1029/97JA02168

Dimmock, A. P., Balikhin, M. A., Krasnoselskikh, V. V., Walker, S. N., Bale, S. D., & Hobara, Y. (2012). A statistical study of the cross-shock electric potential at low mach number, quasi-perpendicular bow shock crossings using cluster data. *Journal of Geophysical Research*, *117*(A2), 2011JA017089. https://doi.org/10.1029/2011JA017089

Formisano, V., & Torbert, R. (1982). Ion acoustic wave forms generated by ion-ion streams at the Earth's bow shock. *Geophysical Research Letters*, *9*(3), 207–210. https://doi.org/10.1029/GL009i003p00207

Fredricks, R. W., Coroniti, F. V., Kennel, C. F., & Scarf, F. L. (1970). Fast time-resolved spectra of electrostatic turbulence in the Earth's bow shock. *Physical Review Letters*, *24*(18), 994–998. https://doi.org/10.1103/PhysRevLett.24.994

Fried, B. D., & Conte, S. D. (1961). *The plasma dispersion function*. Academic Press.

Fuselier, S. A., Gary, S. P., Thomsen, M. F., Bame, S. J., & Gurnett, D. A. (1987). Ion beams and the ion/ion acoustic instability upstream from the Earth's bow shock. *Journal of Geophysical Research*, *92*(A5), 4740–4744. https://doi.org/10.1029/JA092iA05p04740

Gary, S. P., & Omidi, N. (1987). The ion-ion acoustic instability. *Journal of Plasma Physics*, *37*(1), 45–61. https://doi.org/10.1017/S0022377800011983

Gedalin, M. (2020). Preferential heating of heavy ions in shocks. *The Astrophysical Journal*, *900*(2), 171. https://doi.org/10.3847/1538-4357/abaa49

Gedalin, M., Roytershteyn, V., & Pogorelov, N. V. (2023). Shock heating of incident thermal and superthermal populations of different ion species. *The Astrophysical Journal*, *945*(1), 50. https://doi.org/10.3847/1538-4357/acb13a

Goodrich, K. A., Cohen, I. J., Schwartz, S., Wilson, L. B., Turner, D., Caspi, A., et al. (2023). The multi-point assessment of the kinematics of shocks (MAKOS). *Frontiers in Astronomy and Space Sciences*, *10*, 1199711. https://doi.org/10.3389/fspas.2023.1199711

Goodrich, K. A., Ergun, R., Schwartz, S. J., Wilson, L. B., Johlander, A., Newman, D., et al. (2019). Impulsively reflected ions: A plausible mechanism for ion acoustic wave growth in collisionless shocks. *Journal of Geophysical Research: Space Physics*, *124*(3), 1855–1865. https://doi.org/10.1029/2018JA026436

Goodrich, K. A., Ergun, R., Schwartz, S. J., Wilson, L. B., Newman, D., Wilder, F. D., et al. (2018). MMS observations of electrostatic waves in an oblique shock crossing. *Journal of Geophysical Research: Space Physics*, *123*(11), 9430–9442. https://doi.org/10.1029/2018JA025830

Graham, D. B., Khotyaintsev, Y. V., Dimmock, A. P., Lalti, A., Boldú, J. J., Tigik, S. F., & Fuselier, S. A. (2024). Ion dynamics across a low mach number bow shock. *Journal of Geophysical Research: Space Physics*, *129*(4), e2023JA032296. https://doi.org/10.1029/2023JA032296

Graham, D. B., Khotyaintsev, Y. V., & Lalti, A. (2025). Ion-acoustic waves and the proton-alpha streaming instability at collisionless shocks. *Geophysical Research Letters*, *52*(9), e2025GL115273. https://doi.org/10.1029/2025GL115273

Greenstadt, E. W., Russell, C. T., Scarf, F. L., Formisano, V., & Neugebauer, M. (1975). Structure of the quasi-perpendicular laminar bow shock. *Journal of Geophysical Research*, *80*(4), 502–514. https://doi.org/10.1029/JA080i004p00502

Hull, A. J., Larson, D. E., Wilber, M., Scudder, J. D., Mozer, F. S., Russell, C. T., & Bale, S. D. (2006). Large-amplitude electrostatic waves associated with magnetic ramp substructure at Earth's bow shock. *Geophysical Research Letters*, *33*(15), 2005GL025564. https://doi.org/10.1029/2005GL025564

Kamaletdinov, S. R., Vasko, I. Y., & Artemyev, A. V. (2024). Nonlinear electron scattering by electrostatic waves in collisionless shocks. *Journal of Plasma Physics*, *90*(2), 905900201. https://doi.org/10.1017/S0022377824000217

Kasaba, Y., Matsumoto, H., & Omura, Y. (2001). One- and two-dimensional simulations of electron beam instability: Generation of electrostatic and electromagnetic 2 f p waves. *Journal of Geophysical Research*, *106*(A9), 18693–18711. https://doi.org/10.1029/2000JA000329

Kellogg, P. J., Goetz, K., & Monson, S. J. (2010). Harmonics of langmuir waves in the Earth's foreshock. *Journal of Geophysical Research*, *115*(A6), 2009JA014635. https://doi.org/10.1029/2009JA014635

Kellogg, P. J. (2003). Langmuir waves associated with collisionless shocks; a review. *Planetary and Space Science*, *51*(11), 681–691. https://doi.org/10.1016/j.pss.2003.05.001

Kennel, C., Edmiston, J., & Hada, T. (1985). A quarter century of collisionless shock research. *Washington DC American Geophysical Union Geophysical Monograph Series*, *34*, 1–36.

Kucharek, H., Möbius, E., Scholer, M., Mouikis, C., Kistler, L. M., Horbury, T., et al. (2004). On the origin of field-aligned beams at the quasi-perpendicular bow shock: Multi-spacecraft observations by cluster. *Annales Geophysicae*, *22*(7), 2301–2308. https://doi.org/10.5194/angeo-22-2301-2004

Lalti, A., Khotyaintsev, Y. V., Graham, D. B., & Vaivads, A. (2025). Debye-scale electrostatic waves across quasi-perpendicular shocks. *Journal of Geophysical Research: Space Physics*, *130*(7), e2025JA033881. https://doi.org/10.1029/2025JA033881

Lu, X., Vasko, I. Y., & Mozer, F. S. (2025). Electrostatic waves at a quasi-parallel and a quasi-perpendicular interplanetary shock. *Geophysical Research Letters*, *52*(16), e2025GL116649. https://doi.org/10.1029/2025GL116649

Madanian, H., Chen, L.-J., Ng, J., Starkey, M. J., Fuselier, S. A., Bessho, N., et al. (2024). Interaction of the prominence plasma within the magnetic cloud of an interplanetary coronal mass ejection with the Earth's bow shock. *The Astrophysical Journal*, *976*(2), 219. https://doi.org/10.3847/1538-4357/ad8579

Mostafavi, P., Allen, R. C., McManus, M. D., Ho, G. C., Raouafi, N. E., Larson, D. E., et al. (2022). Alpha–proton differential flow of the young solar wind: Parker solar probe observations. *The Astrophysical Journal Letters*, *926*(2), L38. https://doi.org/10.3847/2041-8213/ac51e1

Müller, N., Steinvall, K., Graham, D., & Pusztai, I. (2026). PIC data and scripts for "the proton-alpha instability as a source of ion heating at Earth's bow shock" [Dataset]. *Zenodo*. https://doi.org/10.5281/zenodo.20516745

Muschietti, L., & Lembège, B. (2013). Microturbulence in the electron cyclotron frequency range at perpendicular supercritical shocks. *Journal of Geophysical Research: Space Physics*, *118*(5), 2267–2285. https://doi.org/10.1002/jgra.50224

Onsager, T. G., & Holzworth, R. H. (1990). Measurement of the electron beam mode in Earth's foreshock. *Journal of Geophysical Research*, *95*(A4), 4175–4186. https://doi.org/10.1029/JA095iA04p04175

Pulupa, M., & Bale, S. D. (2008). Structure on interplanetary shock fronts: Type II radio burst source regions. *The Astrophysical Journal*, *676*(2), 1330–1337. https://doi.org/10.1086/526405

Pusztai, I., TenBarge, J. M., Csapó, A. N., Juno, J., Hakim, A., Yi, L., & Fülöp, T. (2018). Low mach-number collisionless electrostatic shocks and associated ion acceleration. *Plasma Physics and Controlled Fusion*, *60*(3), 035004. https://doi.org/10.1088/1361-6587/aaa2cc

Rodriguez, P., & Gurnett, D. A. (1976). Correlation of bow shock plasma wave turbulence with solar wind parameters. *Journal of Geophysical Research (1896-1977)*, *81*(16), 2871–2882. https://doi.org/10.1029/JA081i016p02871

Steinberg, J. T., Lazarus, A. J., Ogilvie, K. W., Lepping, R., & Byrnes, J. (1996). Differential flow between solar wind protons and alpha particles: First WIND observations. *Geophysical Research Letters*, *23*(10), 1183–1186. https://doi.org/10.1029/96GL00628

Vasko, I. Y., Mozer, F. S., Bale, S. D., & Artemyev, A. V. (2022). Ion-acoustic waves in a quasi-perpendicular Earth's bow shock. *Geophysical Research Letters*, *49*(11), e2022GL098640. https://doi.org/10.1029/2022GL098640

Vasko, I. Y., Mozer, F. S., Krasnoselskikh, V. V., Artemyev, A. V., Agapitov, O. V., Bale, S. D., et al. (2018). Solitary waves across supercritical quasi-perpendicular shocks. *Geophysical Research Letters*, *45*(12), 5809–5817. https://doi.org/10.1029/2018GL077835

Walker, S. N., Gedalin, M., & Balikhin, M. A. (2026). Debye-scale bipolar structures and their role in the electron trajectory instability at the bow shock. *Journal of Geophysical Research: Space Physics*, *131*(1), e2025JA034361. https://doi.org/10.1029/2025JA034361

Wang, R., Vasko, I. Y., Mozer, F. S., Bale, S. D., Artemyev, A. V., Bonnell, J. W., et al. (2020). Electrostatic turbulence and debye-scale structures in collisionless shocks. *The Astrophysical Journal Letters*, *889*(1), L9. https://doi.org/10.3847/2041-8213/ab6582

Wang, R., Vasko, I. Y., Mozer, F. S., Bale, S. D., Kuzichev, I. V., Artemyev, A. V., et al. (2021). Electrostatic solitary waves in the Earth's bow shock: Nature, properties, lifetimes, and origin. *Journal of Geophysical Research: Space Physics*, *126*(7), e2021JA029357. https://doi.org/10.1029/2021JA029357

Wilson, L. B., Cattell, C., Kellogg, P. J., Goetz, K., Kersten, K., Hanson, L., et al. (2007). Waves in interplanetary shocks: A Wind/WAVES study. *Physical Review Letters*, *99*(4), 041101. https://doi.org/10.1103/PhysRevLett.99.041101

Wilson, L. B., Cattell, C. A., Kellogg, P. J., Goetz, K., Kersten, K., Kasper, J. C., et al. (2010). Large-amplitude electrostatic waves observed at a supercritical interplanetary shock. *Journal of Geophysical Research*, *115*(A12), 2010JA015332. https://doi.org/10.1029/2010JA015332

Wilson, L. B., Chen, L.-J., & Roytershteyn, V. (2021). The discrepancy between simulation and observation of electric fields in collisionless shocks. *Frontiers in Astronomy and Space Sciences*, *7*, 592634. https://doi.org/10.3389/fspas.2020.592634

Wilson, L. B., Sibeck, D. G., Breneman, A. W., Contel, O. L., Cully, C., Turner, D. L., et al. (2014). Quantified energy dissipation rates in the terrestrial bow shock: 2. Waves and dissipation. *Journal of Geophysical Research: Space Physics*, *119*(8), 6475–6495. https://doi.org/10.1002/2014JA019930

Yang, Z. W., Lembège, B., & Lu, Q. M. (2011). Acceleration of heavy ions by perpendicular collisionless shocks: Impact of the shock front nonstationarity. *Journal of Geophysical Research*, *116*(A10). https://doi.org/10.1029/2011JA016605

Zank, G. P., Pauls, H. L., Cairns, I. H., & Webb, G. M. (1996). Interstellar pickup ions and quasi-perpendicular shocks: Implications for the termination shock and interplanetary shocks. *Journal of Geophysical Research*, *101*(A1), 457–477. https://doi.org/10.1029/95JA02860